ACS APPLIED MATERIALS & INTERFACES

Research Article

www.acsami.org

Sandwichlike Magnesium Silicate/Reduced Graphene Oxide Nanocomposite for Enhanced Pb^{2+} and Methylene Blue Adsorption

Chen-Xi Gui,[†] Qian-Qian Wang,[†] Shu-Meng Hao,[†] Jin Qu,*[,†] Pei-Pei Huang,[‡] Chang-Yan Cao,[‡] Wei-Guo Song,[‡] and Zhong-Zhen Yu*[,†]

[†]State Key Laboratory of Organic–Inorganic Composites, Department of Polymer Engineering, College of Materials Science and Engineering, Beijing University of Chemical Technology, Beijing 100029, China

[‡]Beijing National Laboratory for Molecular Sciences (BNLMS) & Key Laboratory for Molecular Nanostructures and Nanotechnology, Institute of Chemistry, Chinese Academy of Sciences, Beijing 100190, China

Supporting Information

ABSTRACT: A sandwichlike magnesium silicate/reduced graphene oxide nanocomposite (MgSi/RGO) with high adsorption efficiency of organic dye and lead ion was synthesized by a hydrothermal approach. MgSi nanopetals were formed in situ on both sides of RGO sheets. The nanocomposite with good dispersion of nanopetals exhibits a high specific surface area of 450 m^2/g and a good mass transportation property. Compared to MgSi and RGO, the mechanical stability and adsorption capacity of the nanocomposite is significantly improved due to the synergistic effect. The maximum adsorption capacities for methylene blue and lead ion are 433 and 416 mg/g, respectively.

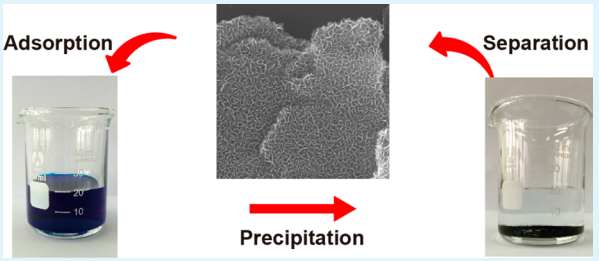

KEYWORDS: *magnesium silicate, reduced graphene oxide, lead ion, nanocomposite, adsorption*

1. INTRODUCTION

Layered nanomaterials have two-dimensional (2D) layered structure with tuned interlayer spaces. Ions and molecules, such as lithium ions, heavy metal ions, or dyes, could transport between layers or exchange with other ions. Because of their outstanding diffusion performance, layered nanomaterials were widely used in nanofillers,[1−3] bionanocomposites,[4,5] energy storage,[6−10] photocatalysts,[11−13] adsorption, and separation.[14−16] As an important type of layered nanomaterial, layered silicates are stable, low cost, and environmentally benign. For example, palygorskite and montmorillonite have been used as adsorbents in water treatment for years. Lead ion (Pb^{2+}) and methylene blue (MB) were widely investigated toxic pollutants in industrial or agriculture wastewater and could cause a wide range of health problems. Drinking water containing these pollutants could cause serious disorders, such as cancer, nausea, coma, and mental retardation.[17−20] Recently, flowerlike zinc silicate nanomaterials with layered structures exhibited a high adsorption capability of Pb^{2+} for water treatment.[21] Magnesium silicate nanotubes also showed excellent adsorption capacities of 929, 424, 362, and 276 mg/g for UO_2^{2+}, Pb^{2+}, Rhodamine B, and MB, respectively.[22] Because of the analogous structure to graphite, layered silicates might also serve as competitive candidates for anode materials in lithium ion batteries. Hydrothermally reduced multiwalled $Ni_3Si_2O_5(OH)_4$ nanotubes were reported to retain a specific capacity of 308.5 (mA h)/g after 21 cycles at a current rate of 20 mA/g.[23] We also designed a novel layered zinc silicate/carbon/reduced graphene oxide (RGO) composite with a three-dimensional (3D) carbon-based conductive network, which exhibited a specific capacity as high as 778 (mA h)/g after 50 cycles.[24]

Hollow structured metal silicates and core–shell structured iron oxide/magnesium silicate composites were reported for water treatment with high adsorption capacities of dyes and metal ions.[25−29] However, all these materials are in the nanoscale, which are difficult to be separated from the solution and might cause secondary pollution. Fabrication of nanomaterials with larger sizes could solve the problem, but the Brunauer–Emmett–Teller (BET) surface area and adsorption performance would decrease accordingly. Combination of layered silicates with other large-scale materials would be an effective approach to obtain a better separation property while retaining the high adsorption capacity.

RGO has been integrated with other inorganic materials to improve the electrochemical or photochemical performances, as the presence of RGO could help to sustain the volume change of the inorganic materials and improve their electron transport property.[30−34] For adsorption application, RGO could serve as a soft buffer to stabilize the inorganic structure and as a separator to prevent the aggregation of inorganic nanomaterials which would decrease the BET surface area and lower the adsorption

Received: June 21, 2014
Accepted: July 29, 2014
Published: July 29, 2014

capacity. RGO could also enhance the adsorption of ions and molecules by electrostatic attraction or conjugation.

In this study, a step-by-step approach was used to synthesize in situ a sandwichlike magnesium silicate (MgSi)/RGO nanocomposite. Silica nanoparticles were grown on RGO sheets as the silicon source, and the sandwichlike MgSi/RGO nanocomposite was synthesized under a mild hydrothermal condition. Improved dispersion of MgSi enhanced mass transportation efficiency and resulted in a large BET surface area (up to 450 m^2/g). When used as adsorbent, the as-prepared sandwichlike MgSi/RGO nanocomposite exhibits excellent removal capabilities of 416 and 433 mg/g for Pb^{2+} and MB, respectively.

2. EXPERIMENTAL SECTION

2.1. Materials. Graphite was purchased from Huadong Graphite Factory (China) with an average diameter of 13 μm. Sulfuric acid (H_2SO_4, 98%), hydrochloric acid (HCl, 37%), hydrogen peroxide (H_2O_2), ammonium hydroxide ($NH_3{\cdot}H_2O$, 28%), magnesium chloride ($MgCl_2{\cdot}6H_2O$), ammonia chloride (NH_4Cl), tetraethyl orthosilicate (TEOS), lead nitrate ($Pb(NO_3)_2$), and MB were bought from Beijing Chemical Factory (China). All chemicals are analytical grade and were used without further purification.

2.2. Synthesis of Silica/RGO Nanocomposite. Silica/RGO nanocomposite was synthesized by a reported sol−gel method.[35] Graphene oxide (GO) (120 mg) was ultrasonicated in ethanol (240 mL) and deionized water (24 mL) for 2 h. $NH_3{\cdot}H_2O$ (4 mL) was then added dropwise and the suspension was ultrasonicated for another 1 h. TEOS (0.5 mL) was added, and the mixture was further ultrasonicated for 3 h. The suspension was rested for 24 h, centrifuged, washed with ethanol for 3 times, and dried at 60 °C in an oven for 12 h.

2.3. Synthesis of MgSi/RGO Nanocomposite. MgSi/RGO nanocomposite was synthesized using a hydrothermal approach.[22] Silica/RGO (50 mg) was dispersed by ultrasonication in 20 mL of deionized water as suspension A. Magnesium chloride (50.8 mg), ammonia chloride (530.5 mg), and $NH_3{\cdot}H_2O$ (1 mL) were dissolved in deionized water (30 mL) as solution B. Suspension A and solution B were mixed and transferred to an autoclave at 140 °C for 8 h. The product was centrifuged, washed with deionized water for several times, and dried in an oven at 60 °C for 6 h. For comparison, GO was treated with a similar hydrothermal method to synthesize RGO. MgSi hollow spheres were synthesized as reported.[26]

2.4. Characterization. X-ray diffraction (XRD) measurement was carried out using a Rigaku D/Max 2500 diffractometer with Cu Kα radiation (λ = 1.54 Å) at a generator voltage of 40 kV and a generator current of 40 mA. MgSi/RGO, RGO, and MgSi were characterized with high-resolution X-ray photoelectron spectroscopy (XPS; Thermo VG RSCAKAB 250X), Fourier transform infrared spectroscopy (FT-IR; Nicolet Nexus 670), and Raman microscopy (Renishaw inVia, Britain). The morphology and microstructure of the nanocomposite were observed with field emission scanning electron microscopy (SEM; Zeiss Supra 55) and transmission electron microscopy (TEM; JEOL JEM-3010). The surface area of the product was measured by a BET method using N_2 adsorption and desorption isotherms on an Autosorb-1 analyzer at 78.3 K. Thermogravimetric analysis (TGA) was conducted on a TA Instruments Q50 thermal analyzer. The concentration of lead ions was analyzed using inductively coupled plasma atomic emission spectroscopy (ICP-AES; Shimadzu ICPE-9000). MB concentration was measured with a Thermal Scientic Evolution 200 UV−visible (UV−vis) spectrophotometer.

2.5. Adsorption Experiments. Pb^{2+} and MB adsorption experiments were carried out with a similar process. In a typical procedure to obtain the adsorption isotherm, 20 mg of MgSi/RGO nanocomposite was mixed with 20 mL of solution of different initial concentrations at room temperature, with no other additives present, and stirred for 12 h to ensure adsorption equilibrium. The adsorbent was removed by centrifugation, and the filtrate was analyzed by ICP-AES or UV−vis spectroscopy.

3. RESULTS AND DISCUSSION

As reported previously,[22] silica nanotubes with mesoporous walls synthesized using hard/soft dual templates could serve as the structure director for fabrication of metal silicate nanotubes, with original tubular structure of the silica nanotubes retained. With these templates, the structure of materials was programmable. To ensure the tight interaction of MgSi with RGO, a two-step approach is designed to synthesize the sandwichlike MgSi/RGO nanocomposite (Figure 1). First, silica nanoparticles are planted

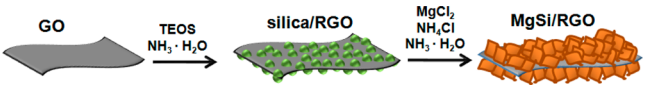

Figure 1. Schematic of the preparation of the sandwichlike MgSi/RGO nanocomposite.

on both sides of GO sheets by the hydrolysis of TEOS in an alkaline medium. During the process, the oxygen-containing groups of GO are connected with silica nanoparticles tightly, as reported in other metal oxide/RGO nanocomposites.[32,36] Second, silica nanoparticles are converted in situ to MgSi nanopetals under a similar hydrothermal condition. The sandwichlike MgSi/RGO nanocomposite is thus obtained.

XRD patterns of GO, MgSi, and MgSi/RGO are shown in Figure 2a. The XRD pattern of GO, which was fabricated with a modified Hummers method,[37,38] shows a typical sharp peak at 2θ = 12° with a corresponding interlayer spacing of 0.74 nm,[39] indicating that a large amount of oxygen-containing functional groups are intercalated into the interlayer space of graphite. This sharp peak is not observed in the XRD pattern of MgSi/RGO, because the silica nanoparticles formed on each side of the RGO by the sol−gel treatment prevent the restacking of these RGO sheets. The peaks of MgSi and MgSi/RGO samples are relatively broadened and overlapped with each other, but all peaks can be indexed to magnesium silicate ($Mg_3Si_4O_9(OH)_{10}$, JCPDS: 03-0174). No other impurities are observed. The morphologies of GO, silica/RGO, and MgSi/RGO are observed with SEM. As reported,[26] the as-prepared MgSi shows a hollow spherical structure with diameters around 500 nm (Figure S1, Supporting Information). Its shell is made of dozens of twisted nanopetals. Figure 2b shows that as-prepared GO exhibits a smooth surface with the size up to the micrometer scale. After the hydrolysis of TEOS, lots of nanoparticles lying on the surface of GO make it relatively rough, confirming the formation of silica nanoparticles (Figure 2c). Some studies have shown that the silica nanomaterials could serve as the silicon source to synthesize the metal silicate.[26,28,40] Here, the anchored silica also serves as the structure director to synthesize in situ MgSi/RGO nanocomposite. After treated with a mild hydrothermal process, the silica on the surface converts to petal-like structure while the nanopetals are still anchored on both sides of the nanocomposite (Figure 2d). RGO sheets could not be observed from the SEM image. Such a large size would make the nanocomposite be separated easily from water thus avoiding secondary pollution. The plate-on-plate sandwichlike structure is studied further by TEM observation. The twisted nanopetals are connected with each other to form a MgSi layer growing on the surface and edge of RGO (Figure 2e). From the edge, RGO is observed between two MgSi layers, indicating a sandwichlike structure. The corresponding selected area electron diffraction analysis indicates that the MgSi is successfully formed in the nanocomposite (Figure 2f).

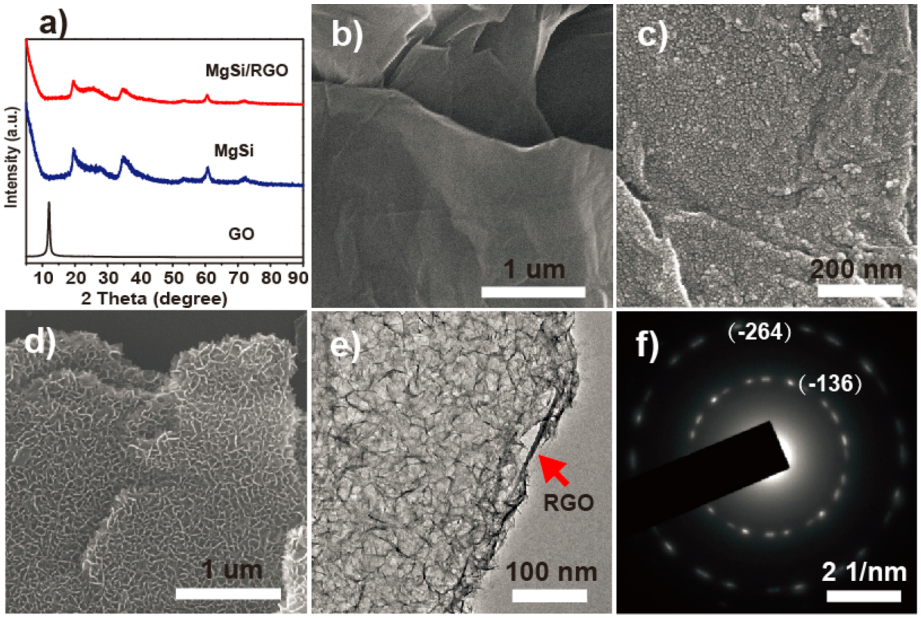

Figure 2. (a) XRD patterns of GO, MgSi, and MgSi/RGO; SEM images of (b) GO, (c) silica/RGO, and (d) MgSi/RGO; (e) TEM image and (f) diffraction pattern of MgSi/RGO.

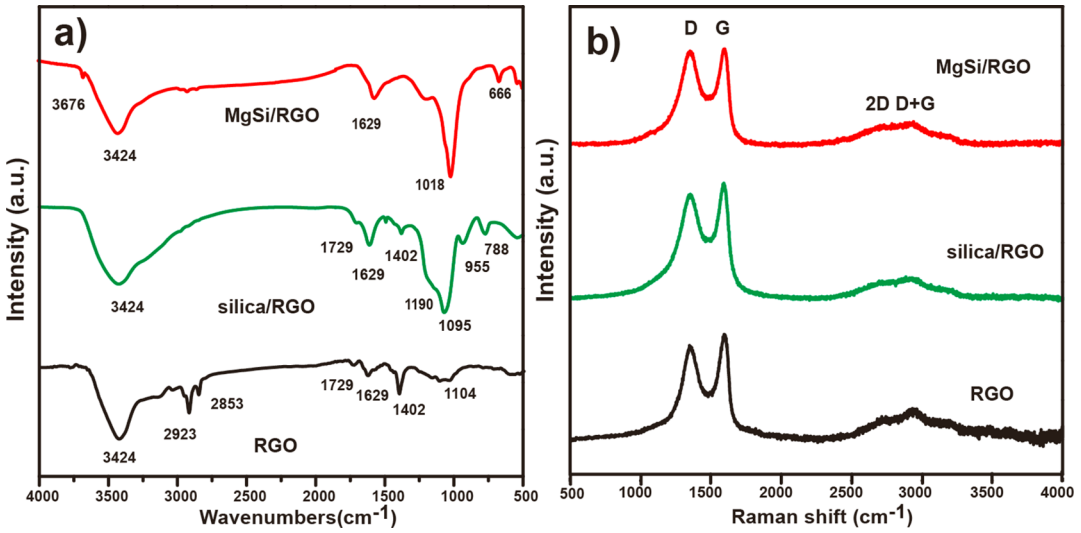

Figure 3. (a) FT-IR spectra and (b) Raman spectra of RGO, silica/RGO, and MgSi/RGO.

FT-IR spectra of RGO, silica/RGO, and MgSi/RGO are shown in Figure 3a. Compared to RGO, the silica/RGO nanocomposite exhibits new bands at 1190, 1095, 955, and 788 cm^{-1}, which are attributed to the stretching and deformation vibrations of coated silica on the surface of RGO.[5,25,35] After the hydrothermal treatment, the presence of new bonds appearing at 3676, 1018, and 666 cm^{-1} for the MgSi/RGO nanocomposite confirms the formation of MgSi.[5,25] The peak at 3424 cm^{-1} could be assigned to the stretching and bending modes of adsorbed water. All these bands could also be observed in the FT-IR spectrum of MgSi (Figure S2, Supporting Information). The band at 1629 cm^{-1} is associated with carboxylate groups of RGO. Raman spectroscopy is a powerful tool to investigate the structural change of carbon materials.[32,36] As shown in Figure 3b, there are two regular peaks corresponding to the D band (ca. 1340 cm^{-1}) and the G band (ca. 1590 cm^{-1}). The G band corresponds to the first-order scattering of the E_{2g} mode observed for sp^2 carbon domains, while the pronounced D band is caused by structural defects or edges that break the symmetry and selection rule. The intensity ratio of the D band to the G band (I_D/I_G) is usually used to measure the graphitization degree of carbon materials. The I_D/I_G value of GO is 0.85; after being composited with silica, the value increases to 0.91, and then, the value further increases to 0.98 for the MgSi/RGO nanocomposite, indicating that not only the silica nanoparticles but also the MgSi nanopetals in the nanocomposite result in the increased disorder degree of RGO sheets. Such a structural change would provide more active sites for adsorption.

To trace the variation in surface composition during each stage of the synthesis, Figure 4 shows XPS spectra of GO, silica/RGO, MgSi/RGO, and MgSi. GO typically shows only carbon and oxygen peaks, with a C/O ratio of 4.98, indicating high levels of oxidation (Figure 4a). The oxygen-containing functional groups are identified by deconvoluting the C 1s and O 1s spectra of GO. The peaks at 284.5, 286.4, and 288.4 eV correspond to C—C, C—O, and C═O moieties, respectively (Figure 4b). The silica

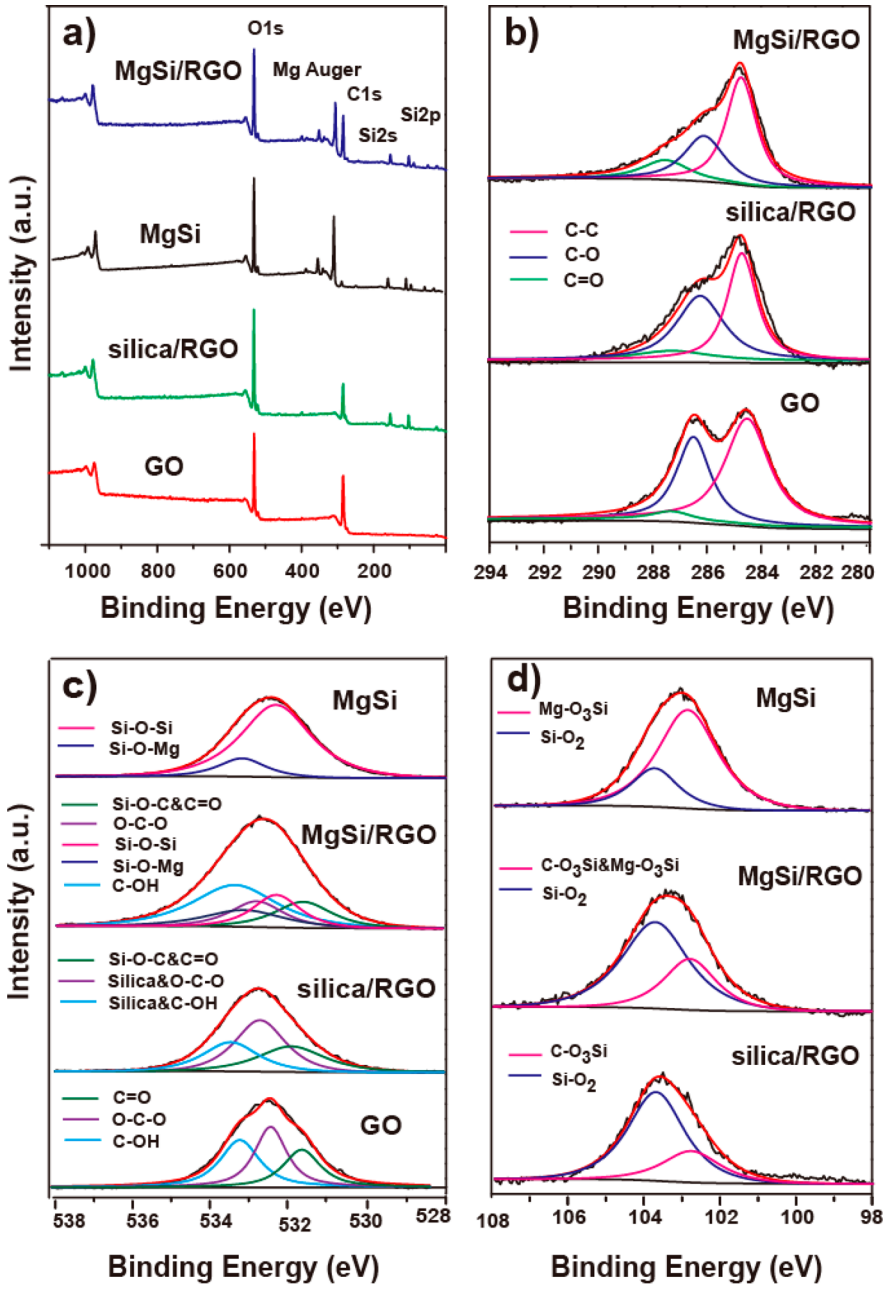

Figure 4. XPS spectra of GO, silica/RGO, MgSi/RGO, and MgSi. (a) Survey scans, (b) C 1s, (c) O 1s, and (d) Si 2p.

nanoparticles on RGO by the sol−gel process result in the presence of the Si peak and the intensity decrease of the oxygen-containing peaks. Curve fitting results of the O 1s and Si 2p spectra, as shown in Figure 4c, d, show that the peaks at approximately 532.5, 533.4, and 103.8 eV are indications of the formation of a silica network.[35] There is a peak at 102.8 eV for Mg−O_3Si in the MgSi hollow sphere, which is overlapped with the C−O_3Si peak in the MgSi/RGO nanocomposite. However, the peaks at 531.7 and 102.8 eV are an evidence of the covalent bonding between the RGO and silica.[35] Some studies have shown that the oxygen bridge bond between the carbon and metal atoms could be formed in the hydrothermal process.[7,32] The strong C−O−Si covalent bonding would not be broken during this mild hydrothermal condition. Hydrothermal treatment of silica/RGO leads to a further intensity decrease of the oxygen-containing functional groups in the C 1s spectra, indicating the reduction of GO to RGO during the treatment. The peak at 532.5 eV moves to 532.3 eV for the Si−O−Si bond and 533.2 eV for the Si−O−Mg bond. It agrees well with the spectrum of MgSi hollow spheres (Figure 4c).

The specific surface area of the MgSi/RGO nanocomposite calculated by the BET method is 450 m^2/g (Figure S3, Supporting Information). Such a high BET surface area is due to the porous MgSi layer with all nanopetals exposed on the surface of RGO sheets. These pores are very likely due to the void spaces formed by the stacking of MgSi nanoplates.[41] For adsorption application, the stability of the nanocomposite in acidic and basic solution should be evaluated. Mg^{2+} concentration is conducted with ICP-AES at the pH range 2−7. The data show that both as-prepared MgSi and MgSi/RGO samples can exist stably within pH 4−7 (Figure 5a). In our study, the pH values of solutions of lead ions are at 5−7 depending on the

dx.doi.org/10.1021/am503997e | ACS Appl. Mater. Interfaces 2014, 6, 14653−14659

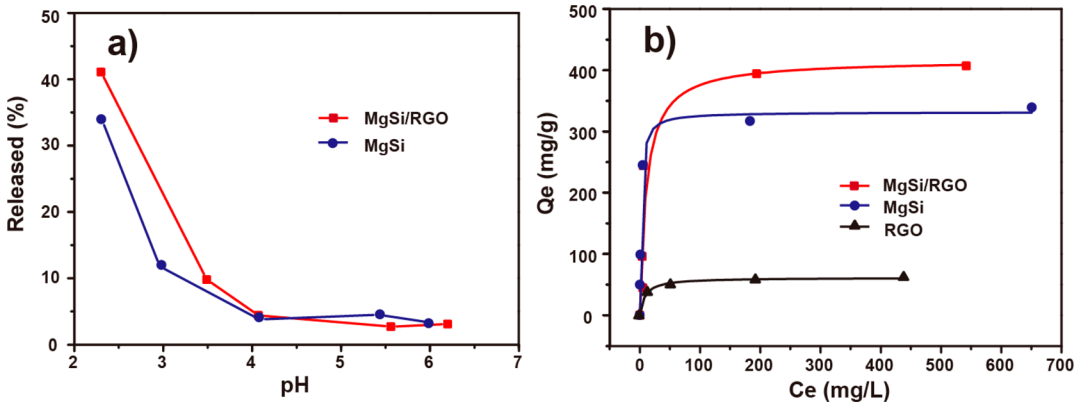

Figure 5. (a) Concentration curves of Mg^{2+} from as-prepared MgSi and MgSi/RGO as a function of pH value; (b) adsorption isotherm of Pb^{2+} on RGO, MgSi, and MgSi/RGO. Ce (mg/L): the equilibrium concentration of the Pb^{2+} solution; Qe (mg/g): the amount of Pb^{2+} adsorbed at equilibrium.

concentration without adjusting. The adsorption properties of various silicate adsorbents are listed in Table 1 for comparison.

Table 1. Pb^{2+} Adsorption Properties of MgSi/RGO and Related Materials Reported in the Literature

adsorbent	BET (m^2/g)	Q_m[a] (mg/g)	Q_m/BET (mg/m^2)	ref
MgSi/RGO	450	416	0.92	this work
RGO	485	61	0.13	this work
MgSNT	604	424	0.70	22
MgSi hollow sphere	521	300	0.58	26
MgSi hollow sphere	470	147	0.31	28
MgSi hollow sphere	355	65	0.18	29
MgSi core–shell sphere	386	48	0.12	29
MgSi nanotubes	222	41	0.18	29

[a] Q_m (mg/g): the maximum adsorption capacity of Pb^{2+}.

To investigate the adsorption capacities, adsorption isotherms of RGO, MgSi, and MgSi/RGO for Pb^{2+} are obtained. The Langmuir model is employed for adsorption analysis:[42,43]

$$Q_e = Q_m bC_e/(1 + bC_e)$$

where C_e is the equilibrium concentration of Pb^{2+} (mg/L), Q_e is the amount of Pb^{2+} adsorbed per unit weight of the adsorbent at equilibrium (mg/g), Q_m (mg/g) is the maximum adsorption capacity, and b is a constant in the Langmuir equation related to the energy of adsorption and the binding strength. The adsorption data of the specimens fit the Langmuir adsorption isotherm well (Figure 5b). The maximum adsorption capacity of the as-prepared MgSi/RGO for Pb^{2+} is 416 mg/g, which is substantially higher than that of RGO (61 mg/g, Figure 5b) and the controlled MgSi hollow spheres (331 mg/g, Figure 5b). Compared with the reported values (Table 1), the MgSi/RGO nanocomposite has a higher or competitive adsorption performance with a moderate BET surface area. However, the MgSi content in the nanocomposite is just 70.3%, which is determined by TGA (Figure S4, Supporting Information). On the basis of this data, the calculated capacity of MgSi in the nanocomposite is up to as high as 566 mg/g, much higher than the reported values in the literature.

In addition, if the adsorption capacity is evaluated based on the surface area, the MgSi/RGO nanocomposite also shows the highest adsorption capacity (0.92 mg/m^2) per unit surface area (Table 1), which is nearly twice that of MgSi hollow spheres and 31.4% higher than that of magnesium silicate nanotubes (MgSNT). Because the capacity of RGO is much lower than that of MgSi hollow spheres, the capacity of the nanocomposite should mainly result from the MgSi component. However, the MgSi/RGO nanocomposite with just 70.3% MgSi shows a much higher capacity than the MgSi hollow sphere alone, indicating that the sandwichlike structure with all nanopetals exposed on the surface exhibits much higher adsorption efficiency than other nanostructured silicate materials. For adsorbents, the surface is where adsorption occurs; a large BET surface area may lead to a high capacity. However, the efficiency of mass transportation, which is related to the structure of materials, is another important factor. Take the controlled MgSi hollow structure as an example,

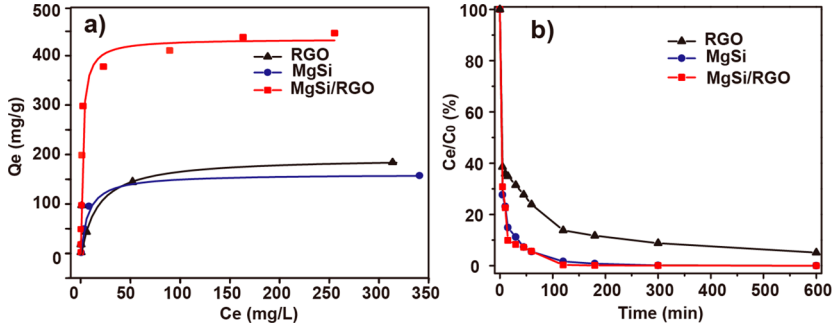

Figure 6. (a) Adsorption isotherm of MB on RGO, MgSi, and MgSi/RGO. Ce (mg/L): the equilibrium concentration of the MB solution; Qe (mg/g): the amount of MB adsorbed at equilibrium. (b) Time-dependent concentration of MB (initial concentration of 100 mg/L) using RGO, MgSi, and MgSi/RGO.

dx.doi.org/10.1021/am503997e | ACS Appl. Mater. Interfaces 2014, 6, 14653–14659

it has a higher BET surface area, and the lead ions in the solution could easily transport and be adsorbed by the outer exposed MgSi through ion exchange. However, because the twisted nanopetals are closely packed to form an about 100 nm thick shell, the ions might be difficult to diffuse to the inner side and react with MgSi. Differently, if the MgSi nanopetals are planted on the surface of RGO sheets, there would be no inner surface, and all the MgSi nanopetals are exposed to the solution, benefiting the adsorption of Pb^{2+}. Therefore, the sandwichlike MgSi/RGO nanocomposite exhibits a higher adsorption capacity.

Besides serving as a soft buffer to disperse the MgSi nanopetals to fully expose their active sites, RGO also serves as a separator to avoid the nanopetals to suffer from their aggregation, which leads to a huge loss of surface area, thus damaging the adsorption property. As detected by XPS, the Si−O−C bond between RGO and MgSi enhances its mechanical stability. After a long time mechanical stirring and ultrasonic treatment, the structure is still well preserved (Figure S5, Supporting Information). In addition, the micrometer-scale nanocomposite can be easily separated by gravity (Figure S6, Supporting Information). RGO can also adsorb ions and molecules through electrostatic attraction or conjugation with the oxygen-containing functional groups.

The adsorption of MB is also investigated. Figure 6a shows that the adsorption data fit the Langmuir adsorption isotherm well. The maximum adsorption capacity of the as-prepared MgSi/RGO nanocomposite for MB is 433 mg/g, while the maximum adsorption capacities of RGO and MgSi reach only 195 and 160 mg/g, respectively. The value of 433 mg/g is also much higher than that of MgSNT. The time-dependent experiment shows that the nanocomposite has a faster adsorption rate of MB at room temperature than the controlled samples under the initial concentration of 100 mg/L (Figure 6b). Although the BET surface area of the MgSi/RGO nanocomposite is 450 m^2/g, which is lower than that of MgSi (521 m^2/g), the nanocomposite still had a similar adsortpion rate to MgSi alone. It was reported that the adsorption process of GO composites followed the pseudo-second-order rate adsorption kinetic model,[44,45] which is also in agreement with our results. As shown in Table S1, Supporting Information (the data are fitted based on Figure 6b, so Q_e is lower than their maximum adsorption capacities), the correlation coefficients of the samples are almost 1. The adsorption rate of the MgSi/RGO nanocomposite is a little higher than that of MgSi. It means the adsorption capacity is affected not only by BET surface area but also the efficiency of mass transportation that is related to the structure of materials. These results indicate that the layer-by-layer structure can serve as a highly efficient adsorbent in the application of water treatment. Meanwhile, the adsorption capacity of MgSi/RGO toward $Cr_2O_7^{2-}$ is also measured, and nearly no adsorption is observed. This is because the surfaces of MgSi and MgSi/RGO nanocomposite are negatively charged in aqueous solution with pH value of about 7[26] and the anions such as $Cr_2O_7^{2-}$ cannot be adsorbed.

4. CONCLUSION

MgSi/RGO nanocomposite is synthesized by a hydrothermal approach. XRD pattern and FT-IR spectra clearly index the crystallographic information on the nanocomposite. XPS results confirm the reduction of GO during the two-step reaction and the existence of a Si−O−C bond that improves the stability of the nanocomposite. SEM and TEM observations show the good dispersion of MgSi nanopetals on RGO sheets to form a 2D sandwichlike composited structure. The improved dispersion of MgSi and enhanced mass transportation efficiency make the MgSi/RGO nanocomposite high adsorption capacities of 416 and 433 mg/g for Pb^{2+} and MB, respectively. The synergistic effect is well illustrated by increasing the MB and Pb^{2+} adsorption capacities of MgSi alone by 171% and 26%, respectively. This new material would have good potential in water remediation. Such a 2D plates-on-plates composited structure would be an effective approach to improve the mass transportation efficiency of materials for enhanced adsorption ability, catalytic, or lithium ion storage property.

■ ASSOCIATED CONTENT

Supporting Information

SEM image and FT-IR spectrum of MgSi hollow spheres; N_2 adsorption/desorption isotherm for the MgSi/RGO nanocomposite; TGA curves of GO, MgSi, silica/RGO, and MgSi/RGO; SEM image of the MgSi/RGO after a long time mechanical stirring and ultrasonic treatment; digital image of the nanocomposite separated by gravity; kinetic parameters of the pseudo-second-order equation for MB adsorption on MgSi/RGO, MgSi, and RGO. This material is available free of charge via the Internet at http://pubs.acs.org.

■ AUTHOR INFORMATION

Corresponding Authors

*(J.Q.) Fax: +86-10-64428582; e-mail: qujin@mail.buct.edu.cn.
*(Z.-Z.Y.) E-mail: yuzz@mail.buct.edu.cn.

Notes

The authors declare no competing financial interest.

■ ACKNOWLEDGMENTS

Financial support from the National Natural Science Foundation of China (51125010), the National Basic Research Program of China (2011CB933700), the Fundamental Research Funds for the Central Universities, and the State Key Laboratory of Organic−Inorganic Composites (201404) is gratefully acknowledged.

■ REFERENCES

(1) Wang, Q.; Mynar, J. L.; Yoshida, M.; Lee, E.; Lee, M.; Okuro, K.; Kinbara, K.; Aida, T. High-Water-Content Mouldable Hydrogels by Mixing Clay and a Dendritic Molecular Binder. *Nature* **2010**, *463*, 339−343.

(2) Martin, J. E.; Patil, A. J.; Butler, M. F.; Mann, S. Guest-Molecule-Directed Assembly of Mesostructured Nanocomposite Polymer/Organoclay Hydrogels. *Adv. Funct. Mater.* **2011**, *21*, 674−681.

(3) Zhuk, A.; Mirza, R.; Sukhishvili, S. Multiresponsive Clay-Containing Layer-by-Layer Films. *ACS Nano* **2011**, *5*, 8790−8799.

(4) Ruiz-Hitzky, E.; Darder, M.; Aranda, P.; del Burgo, M. A. M.; del Real, G. Bionanocomposites as New Carriers for Influenza Vaccines. *Adv. Mater.* **2009**, *21*, 4167−4171.

(5) Wan, C.; Chen, B. Synthesis and Characterization of Biomimetic Hydroxyapatite/Sepiolite Nanocomposites. *Nanoscale* **2011**, *3*, 693−700.

(6) Wang, L.; Dong, Z. H.; Wang, Z. G.; Zhang, F. X.; Jin, J. Layered α-$Co(OH)_2$ Nanocones as Electrode Materials for Pseudocapacitors: Understanding the Effect of Interlayer Space on Electrochemical Activity. *Adv. Funct. Mater.* **2013**, *23*, 2758−2764.

(7) Qu, J.; Yin, Y. X.; Wang, Y. Q.; Yan, Y.; Guo, Y. G.; Song, W. G. Layer Structured α-Fe_2O_3 Nanodisk/Reduced Graphene Oxide Composites as High-Performance Anode Materials for Lithium-Ion Batteries. *ACS Appl. Mater. Interfaces* **2013**, *5*, 3932−3936.

(8) Liu, J.; Chen, J. S.; Wei, X.; Lou, X. W.; Liu, X. W. Sandwich-like, Stacked Ultrathin Titanate Nanosheets for Ultrafast Lithium Storage. *Adv. Mater.* **2011**, *23*, 998−1002.
(9) Hwang, H.; Kim, H.; Cho, J. MoS_2 Nanoplates Consisting of Disordered Graphene-like Layers for High Rate Lithium Battery Anode Materials. *Nano Lett.* **2011**, *11*, 4826−4830.
(10) Chang, K.; Chen, W.; Ma, L.; Li, H.; Li, H.; Huang, F.; Xu, Z.; Zhang, Q.; Lee, J. Y. Graphene-like MoS_2/Amorphous Carbon Composites with High Capacity and Excellent Stability as Anode Materials for Lithium Ion Batteries. *J. Mater. Chem.* **2011**, *21*, 6251−6257.
(11) Yu, H.; Tian, B.; Zhang, J. Layered TiO_2 Composed of Anatase Nanosheets with Exposed {001} Facets: Facile Synthesis and Enhanced Photocatalytic Activity. *Chem.—Eur. J.* **2011**, *17*, 5499−5502.
(12) Qu, J.; Yu, Y.; Cao, C. Y.; Song, W. G. α-Fe_2O_3 Nanodisks: Layered Structure, Growth Mechanism, and Enhanced Photocatalytic Property. *Chem.—Eur. J.* **2013**, *19*, 11172−11177.
(13) Gunjakar, J. L.; Kim, T. W.; Kim, H. N.; Kim, I. Y.; Hwang, S.-J. Mesoporous Layer-by-Layer Ordered Nanohybrids of Layered Double Hydroxide and Layered Metal Oxide: Highly Active Visible Light Photocatalysts with Improved Chemical Stability. *J. Am. Chem. Soc.* **2011**, *133*, 14998−15007.
(14) Yang, D.; Zheng, Z.; Liu, H.; Zhu, H.; Ke, X.; Xu, Y.; Wu, D.; Sun, Y. Layered Titanate Nanofibers as Efficient Adsorbents for Removal of Toxic Radioactive and Heavy Metal Ions from Water. *J. Phys. Chem. C* **2008**, *112*, 16275−16280.
(15) Komarneni, S.; Kozai, N.; Paulus, W. J. Superselective Clay for Radium Uptake. *Nature* **2001**, *410*, 771−771.
(16) Ide, Y.; Ochi, N.; Ogawa, M. Effective and Selective Adsorption of Zn^{2+} from Seawater on a Layered Silicate. *Angew. Chem., Int. Ed.* **2011**, *123*, 680−682.
(17) Sun, H.; Cao, L.; Lu, L. Magnetite/Reduced Graphene Oxide Nanocomposites: One Step Solvothermal Synthesis and Use as a Novel Platform for Removal of Dye Pollutants. *Nano Res.* **2011**, *4*, 550−562.
(18) Zhao, G.; Ren, X.; Gao, X.; Tan, X.; Li, J.; Chen, C.; Huang, Y.; Wang, X. Removal of Pb(II) Ions from Aqueous Solutions on Few-Layered Graphene Oxide Nanosheets. *Dalton Trans.* **2011**, *40*, 10945−10952.
(19) Yang, S. T.; Chen, S.; Chang, Y.; Cao, A.; Liu, Y.; Wang, H. Removal of Methylene Blue from Aqueous Solution by Graphene Oxide. *J. Colloid Interface Sci.* **2011**, *359*, 24−29.
(20) Huang, Z. H.; Zheng, X.; Lv, W.; Wang, M.; Yang, Q. H.; Kang, F. Adsorption of Lead(II) Ions from Aqueous Solution on Low-Temperature Exfoliated Graphene Nanosheets. *Langmuir* **2011**, *27*, 7558−7562.
(21) Qu, J.; Cao, C. Y.; Hong, Y. L.; Chen, C. Q.; Zhu, P. P.; Song, W. G.; Wu, Z. Y. New Hierarchical Zinc Silicate Nanostructures and Their Application in Lead Ion Adsorption. *J. Mater. Chem.* **2012**, *22*, 3562−3567.
(22) Qu, J.; Li, W.; Cao, C. Y.; Yin, X. J.; Zhao, L.; Bai, J.; Qin, Z.; Song, W. G. Metal Silicate Nanotubes with Nanostructured Walls as Superb Adsorbents for Uranyl Ions and Lead Ions in Water. *J. Mater. Chem.* **2012**, *22*, 17222−17226.
(23) Yang, Y.; Liang, Q.; Li, J.; Zhuang, Y.; He, Y.; Bai, B.; Wang, X. $Ni_3Si_2O_5(OH)_4$ Multi-Walled Nanotubes with Tunable Magnetic Properties and Their Application as Anode Materials for Lithium Batteries. *Nano Res.* **2011**, *4*, 882−890.
(24) Qu, J.; Yan, Y.; Yin, Y. X.; Guo, Y. G.; Song, W. G. Improving the Li-Ion Storage Performance of Layered Zinc Silicate through the Interlayer Carbon and Reduced Graphene Oxide Networks. *ACS Appl. Mater. Interfaces* **2013**, *5*, 5777−5782.
(25) Zhang, S.; Xu, W.; Zeng, M.; Li, J.; Li, J.; Xu, J.; Wang, X. Superior Adsorption Capacity of Hierarchical Iron Oxide@Magnesium Silicate Magnetic Nanorods for Fast Removal of Organic Pollutants from Aqueous Solution. *J. Mater. Chem. A* **2013**, *1*, 11691−11697.
(26) Wang, Y. Q.; Wang, G. Z.; Wang, H. Q.; Liang, C. H.; Cai, W. P.; Zhang, L. D. Chemical-Template Synthesis of Micro/Nanoscale Magnesium Silicate Hollow Spheres for Waste-Water Treatment. *Chem.—Eur. J.* **2010**, *16*, 3497−3503.
(27) Yang, Y.; Zhuang, Y. A.; He, Y. H.; Bai, B.; Wang, X. Fine Tuning of the Dimensionality of Zinc Silicate Nanostructures and Their Application as Highly Efficient Absorbents for Toxic Metal Ions. *Nano Res.* **2010**, *3*, 581−593.
(28) Zheng, J.; Wu, B. H.; Jiang, Z. Y.; Kuang, Q.; Fang, X. L.; Xie, Z. X.; Huang, R. B.; Zheng, L. S. General and Facile Syntheses of Metal Silicate Porous Hollow Nanostructures. *Chem.—Asian J.* **2010**, *5*, 1439−1444.
(29) Zhuang, Y.; Yang, Y.; Xiang, G. L.; Wang, X. Magnesium Silicate Hollow Nanostructures as Highly Efficient Absorbents for Toxic Metal Ions. *J. Phys. Chem. C* **2009**, *113*, 10441−10445.
(30) Tao, S.; Yue, W.; Zhong, M.; Chen, Z.; Ren, Y. Fabrication of Graphene-Encapsulated Porous Carbon−Metal Oxide Composites as Anode Materials for Lithium-Ion Batteries. *ACS Appl. Mater. Interfaces* **2014**, *6*, 6332−6339.
(31) Zhou, X.; Yin, Y. X.; Wan, L. J.; Guo, Y. G. Self-Assembled Nanocomposite of Silicon Nanoparticles Encapsulated in Graphene through Electrostatic Attraction for Lithium-Ion Batteries. *Adv. Energy Mater.* **2012**, *2*, 1086−1090.
(32) Zhou, G.; Wang, D. W.; Yin, L. C.; Li, N.; Li, F.; Cheng, H. M. Oxygen Bridges between NiO Nanosheets and Graphene for Improvement of Lithium Storage. *ACS Nano* **2012**, *6*, 3214−3223.
(33) Xue, D. J.; Xin, S.; Yan, Y.; Jiang, K. C.; Yin, Y. X.; Guo, Y. G.; Wan, L. J. Improving the Electrode Performance of Ge through Ge@C Core−Shell Nanoparticles and Graphene Networks. *J. Am. Chem. Soc.* **2012**, *134*, 2512−2515.
(34) Xin, S.; Guo, Y. G.; Wan, L. J. Nanocarbon Networks for Advanced Rechargeable Lithium Batteries. *Acc. Chem. Res.* **2012**, *45*, 1759−1769.
(35) Hsiao, M. C.; Ma, C. C. M.; Chiang, J. C.; Ho, K. K.; Chou, T. Y.; Xie, X.; Tsai, C. H.; Chang, L. H.; Hsieh, C. K. Thermally Conductive and Electrically Insulating Epoxy Nanocomposites with Thermally Reduced Graphene Oxide−Silica Hybrid Nanosheets. *Nanoscale* **2013**, *5*, 5863−5871.
(36) Zhou, J.; Song, H.; Ma, L.; Chen, X. Magnetite/Graphene Nanosheet Composites: Interfacial Interaction and Its Impact on the Durable High-Rate Performance in Lithium-Ion Batteries. *RSC Adv.* **2011**, *1*, 782−791.
(37) Hummers, W. S., Jr.; Offeman, R. E. Preparation of Graphitic Oxide. *J. Am. Chem. Soc.* **1958**, *80*, 1339−1339.
(38) Tang, X. Z.; Li, W.; Yu, Z. Z.; Rafiee, M. A.; Rafiee, J.; Yavari, F.; Koratkar, N. Enhanced Thermal Stability in Graphene Oxide Covalently Functionalized with 2-Amino-4,6-didodecylamino-1,3,5-triazine. *Carbon* **2011**, *49*, 1258−1265.
(39) Pu, X.; Zhang, H. B.; Li, X.; Gui, C.; Yu, Z. Z. Thermally Conductive and Electrically Insulating Epoxy Nanocomposites with Silica-Coated Graphene. *RSC Adv.* **2014**, *4*, 15297−15303.
(40) Park, J. C.; Lee, H. J.; Bang, J. U.; Park, K. H.; Song, H. Chemical Transformation and Morphology Change of Nickel-Silica Hybrid Nanostructures via Nickel Phyllosilicates. *Chem. Commun.* **2009**, 7345−7347.
(41) Cao, C. Y.; Chen, C. Q.; Li, W.; Song, W. G.; Cai, W. Nanoporous Nickel Spheres as Highly Active Catalyst for Hydrogen Generation from Ammonia Borane. *ChemSusChem* **2010**, *3*, 1241−1244.
(42) Zhong, L. S.; Hu, J. S.; Liang, H. P.; Cao, A. M.; Song, W. G.; Wan, L. J. Self-Assembled 3D Flowerlike Iron Oxide Nanostructures and Their Application in Water Treatment. *Adv. Mater.* **2006**, *18*, 2426−2431.
(43) Cao, Q.; Huang, F.; Zhuang, Z.; Lin, Z. A Study of the Potential Application of Nano-$Mg(OH)_2$ in Adsorbing Low Concentrations of Uranyl Tricarbonate from Water. *Nanoscale* **2012**, *4*, 2423−2430.
(44) Chandra, V.; Park, J.; Chun, Y.; Lee, J. W.; Hwang, I. C.; Kim, K. S. Water-Dispersible Magnetite-Reduced Graphene Oxide Composites for Arsenic Removal. *ACS Nano* **2010**, *4*, 3979−3986.
(45) Sitko, R.; Turek, E.; Zawisza, B.; Malicka, E.; Talik, E.; Heimann, J.; Gagor, A.; Feist, B.; Wrzalik, R. Adsorption of Divalent Metal Ions from Aqueous Solutions Using Graphene Oxide. *Dalton Trans.* **2013**, *42*, 5682−5689.